LETTER

https://doi.org/10.1038/s41586-019-1603-7

PdMo bimetallene for oxygen reduction catalysis

Mingchuan Luo[1,2], Zhonglong Zhao[3], Yelong Zhang[1], Yingjun Sun[1], Yi Xing[1], Fan Lv[1], Yong Yang[1], Xu Zhang[3], Sooyeon Hwang[4], Yingnan Qin[1], Jing-Yuan Ma[5], Fei Lin[1], Dong Su[4], Gang Lu[3] & Shaojun Guo[1,2,6,7]*

The efficient interconversion of chemicals and electricity through electrocatalytic processes is central to many renewable-energy initiatives. The sluggish kinetics of the oxygen reduction reaction (ORR) and the oxygen evolution reaction (OER)[1–4] has long posed one of the biggest challenges in this field, and electrocatalysts based on expensive platinum-group metals are often required to improve the activity and durability of these reactions. The use of alloying[5–7], surface strain[8–11] and optimized coordination environments[12] has resulted in platinum-based nanocrystals that enable very high ORR activities in acidic media; however, improving the activity of this reaction in alkaline environments remains challenging because of the difficulty in achieving optimized oxygen binding strength on platinum-group metals in the presence of hydroxide. Here we show that PdMo bimetallene—a palladium–molybdenum alloy in the form of a highly curved and sub-nanometre-thick metal nanosheet—is an efficient and stable electrocatalyst for the ORR and the OER in alkaline electrolytes, and shows promising performance as a cathode in Zn–air and Li–air batteries. The thin-sheet structure of PdMo bimetallene enables a large electrochemically active surface area (138.7 square metres per gram of palladium) as well as high atomic utilization, resulting in a mass activity towards the ORR of 16.37 amperes per milligram of palladium at 0.9 volts versus the reversible hydrogen electrode in alkaline electrolytes. This mass activity is 78 times and 327 times higher than those of commercial Pt/C and Pd/C catalysts, respectively, and shows little decay after 30,000 potential cycles. Density functional theory calculations reveal that the alloying effect, the strain effect due to the curved geometry, and the quantum size effect due to the thinness of the sheets tune the electronic structure of the system for optimized oxygen binding. Given the properties and the structure–activity relationships of PdMo metallene, we suggest that other metallene materials could show great promise in energy electrocatalysis.

Suprathin PdMo nanosheets were synthesized using a one-pot wet-chemical approach, in which a homogenous solution of palladium(II) acetylacetonate ($Pd(acac)_2$), molybdenum(VI) carbonyl ($Mo(CO)_6$), ascorbic acid and oleylamine was heated at 80 °C for 12 h. As a control, monometallic Pd nanosheets with a similar structure were obtained using the same protocol but with the replacement of $Mo(CO)_6$ by CO (Methods). High-angle annular dark-field scanning transmission electron microscopy (HAADF-STEM) images of PdMo nanosheets show that the product is dominated by two-dimensional (2D) nanosheets with an average lateral size of around 100 nm (Fig. 1a). Owing to its structural analogy with graphene, we herein denote the PdMo nanosheet as 'PdMo bimetallene'. High-magnification HAADF-STEM and TEM images reveal that the as-synthesized nanosheet is highly curved—evidence of its flexibility and suprathin character (Fig. 1b, c). Further evidence for the suprathin character of PdMo bimetallene is its high sensitivity to irradiation by the electron beam during high-voltage or high-resolution TEM experiments (Extended Data Fig. 1a, b). The average thickness of PdMo bimetallene was determined by atomic force microscopy (AFM) to be 0.88 nm (Fig. 1d, e); this is in close agreement with the result obtained using high-resolution TEM (HRTEM; Extended Data Fig. 1c, d). The HRTEM image of PdMo bimetallene shows a lattice spacing of 0.23 nm (Fig. 1c, inset), which is slightly larger than that of the Pd (111) facet. The atomic-resolution HAADF-STEM image and the corresponding fast Fourier transform pattern suggest that PdMo bimetallene is in a cubic phase with a dominant (111) facet (Fig. 1f). STEM elemental mapping shows the homogenous distribution of palladium and molybdenum throughout the metallene (Fig. 1g). The Pd/Mo ratio was determined by inductively coupled plasma atomic emission spectroscopy (ICP–AES) to be 87.8/12.2, which is consistent with the result obtained using TEM energy-dispersive X-ray spectroscopy (TEM–EDX; Extended Data Fig. 1e).

Powder X-ray diffraction (PXRD) patterns show that both Pd metallene and PdMo bimetallene have a face-centred cubic structure (Fig. 1h). The diffraction peaks of Pd metallene are negatively shifted compared with those of commercial carbon-supported palladium nanoparticles (Pd/C), which suggests that Pd metallene has the higher lattice parameter. The addition of molybdenum—which has a larger atomic radius—into the palladium lattice in the case of PdMo bimetallene induces a further negative shift of the diffraction peaks, indicating the formation of alloys. Combining the PXRD results with those from extended X-ray absorption fine structure (EXAFS) analysis (Extended Data Fig. 1f), we estimate a tensile strain of 1.4% for PdMo bimetallene (Methods)[13], resulting from both the curved geometry and the presence of molybdenum. Classical molecular dynamics simulations of PdMo bimetallene at room temperature further reveal that the curved PdMo bimetallene has an average tensile strain of 0.95% (Extended Data Fig. 1g, h), in agreement with the experimental results.

X-ray photoelectron spectroscopy (XPS) confirms the presence of palladium and molybdenum in PdMo bimetallene, and of only palladium in Pd metallene (Fig. 1i, Extended Data Fig. 1i). The core-level Pd 3*d* XPS spectra reveal that palladium in both metallene materials is mainly in its metallic state, whereas nearly half of the palladium in Pd/C is oxidized (Fig. 1i). The latter reflects the fact that a large proportion of the palladium atoms in these supported nanoparticles are under-coordinated edge and corner atoms, which are more oxyphilic than atoms on facets[14]. The shift of the two Pd 3*d* XPS peaks of PdMo bimetallene to higher binding energy relative to those of Pd metallene indicates a downshift of the *d*-band centre in the bimetallene; this is in line with the behaviour of previously reported alloy systems based on platinum-group metals (PGMs)[15,16]. The 3*d* core-level XPS spectrum of molybdenum shows that it is mainly in its metallic state in PdMo bimetallene (Extended Data Fig. 1i); by contrast, the Mo^{6+} and Mo^{4+} states were dominant in previously reported molybdenum-doped nanoparticles with high ORR activity[17]. Given the ease with which molybdenum is oxidized, we infer that the molybdenum atoms are buried inside the PdMo bimetallene. This conclusion is further supported by the absence of galvanic replacement of molybdenum by copper (Methods, Extended Data Fig. 1j).

The synthesis of anisotropic 2D nanostructures is thermodynamically unfavourable because of their high surface free energies[18].

[1]Department of Materials Science and Engineering, College of Engineering, Peking University, Beijing, China. [2]BIC-ESAT, College of Engineering, Peking University, Beijing, China. [3]Department of Physics and Astronomy, California State University, Northridge, CA, USA. [4]Center for Functional Nanomaterials, Brookhaven National Laboratory, Upton, NY, USA. [5]Shanghai Synchrotron Radiation Facility, Shanghai Institute of Applied Physics, Chinese Academy of Sciences, Shanghai, China. [6]Department of Energy and Resources Engineering, College of Engineering, Peking University, Beijing, China. [7]Key Laboratory of Theory and Technology of Advanced Batteries Materials, College of Engineering, Peking University, Beijing, China. *e-mail: guosj@pku.edu.cn

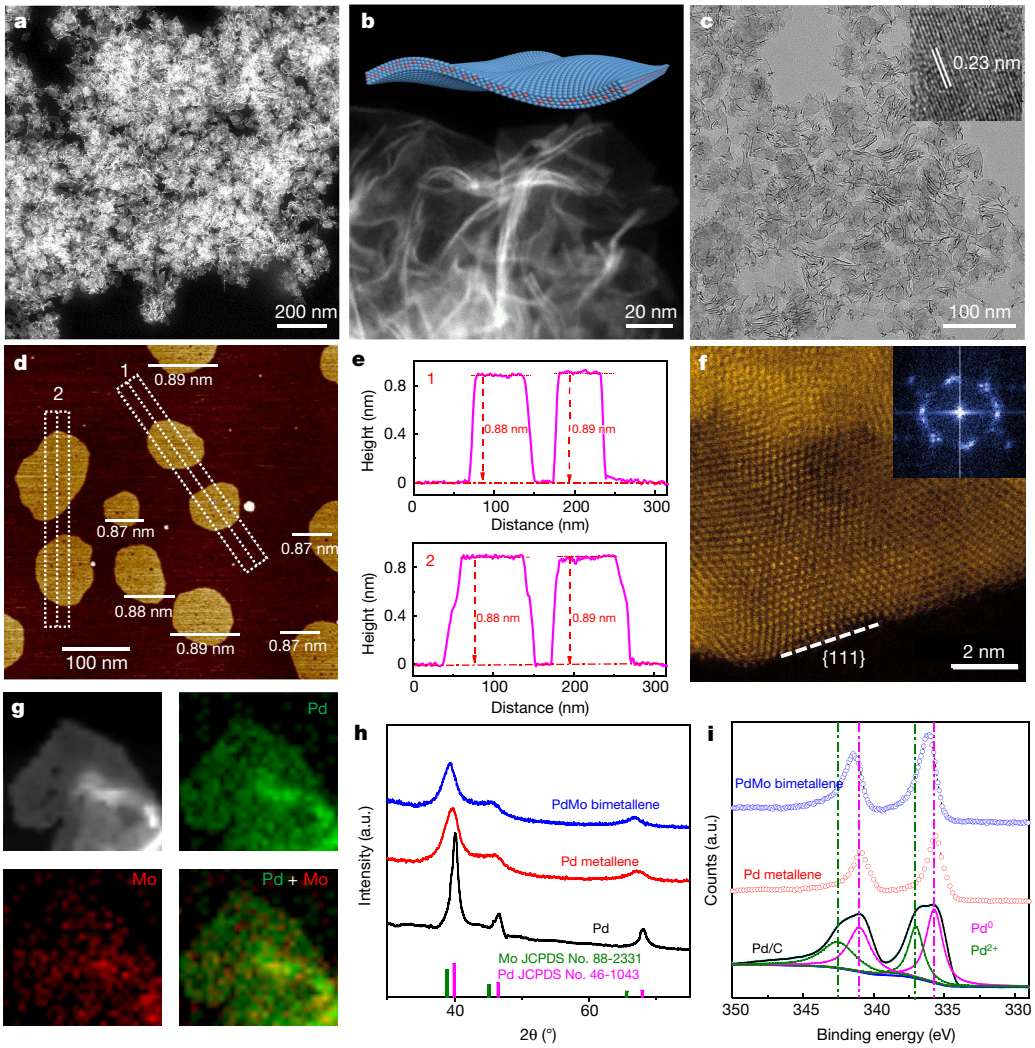

Fig. 1 | Characterization of the morphology, structure and composition of PdMo bimetallene. a–**c**, Low-magnification HAADF-STEM (**a**), high-magnification HAADF-STEM (**b**) and TEM (**c**) images of PdMo bimetallene. The inset of **c** shows an HRTEM image of PdMo bimetallene. **d**, **e**, AFM image (**d**) and corresponding height profiles (**e**) of PdMo bimetallene. **f**, High-resolution HAADF-STEM image taken from a single bimetallene nanosheet. Inset, the corresponding fast Fourier transform patterns. **g**, EDS elemental mapping of palladium and molybdenum in a single bimetallene nanosheet. **h**, **i**, PXRD patterns (**h**) and XPS spectra (**i**) of commercial Pd/C, Pd metallene and PdMo bimetallene catalysts.

Although metallic nanosheets with thicknesses of several nanometres have been prepared using wet-chemical approaches[19–22], access to sub-nanometre multimetallic nanosheets has required the use of polymer surfactants such as polyvinylpyrrolidone (PVP), which is detrimental to catalysis by blocking active sites. We succeeded in producing 0.88-nm-thick free-standing PdMo bimetallene, with a distinctively curved geometry, by carefully controlling the anisotropic growth kinetics through the low-temperature decomposition of the metal carbonyl precursor and the use of a moderately reducing environment. Preparation under less controlled conditions resulted in the formation of non-uniform nanosheets or other products (Extended Data Fig. 2a–h). Ultra-large metallene (with lateral size of several hundreds of nanometres) was obtained when using a high concentration of metal precursors, which indicates an ability to control the lateral size (Extended Data Fig. 2i, j). Our approach also enables the synthesis of PdW bimetallene simply by using $W(CO)_6$ instead of $Mo(CO)_6$ (Extended Data Fig. 2k–o).

To study the growth mechanism of PdMo bimetallene, we characterized the morphologies, compositions and optical adsorption properties of reaction intermediates collected at different stages of the reaction using TEM, TEM–EDX and ultraviolet–visible (UV–vis) absorption spectroscopy, respectively (Extended Data Fig. 3). The evolution of these properties suggests the initial formation of small, pure-Pd nanosheets, with subsequent formation of PdMo bimetallene nanosheets by seed-mediated growth along the lateral direction and diffusion of molybdenum atoms into the metallene.

To test the electrocatalytic capabilities of our metallene materials, we deposited free-standing 2D nanocrystals onto carbon black and compared their performance against that of commercial Pt/C and Pd/C catalysts. In the cyclic voltammograms, the peaks of underpotentially deposited hydrogen (H_{upd}) in the metallene catalysts are larger than those in the Pt/C and Pd/C catalysts (Extended Data Fig. 4a–d), indicating that the thin 2D nanocrystals of the metallenes enable greater utilization of the PGM. Additionally, the H_{upd} peak of PdMo bimetallene/C is negatively shifted relative to that of Pd metallene/C, suggesting weaker adsorption of hydrogen on PdMo bimetallene/C. The weakened adsorptive strength of palladium and the modification of its electronic structure upon alloying with molybdenum are consistent with the XPS results (Fig. 1i). Previous studies of Pt-skin/Pt_3Ni(111) showed a similar suppression of H_{upd} due to subsurface nickel, which resulted in enhanced ORR activity[23,24]. The positive shift in the hydroxide adsorption and oxide reduction peaks of PdMo bimetallene relative to those of Pd metallene confirms the weakened Pd–O binding upon the introduction of molybdenum (Extended Data Fig. 4a, b).

The electrochemically active surface areas (ECSAs) of the various catalysts were determined by means of H_{upd}, CO stripping,

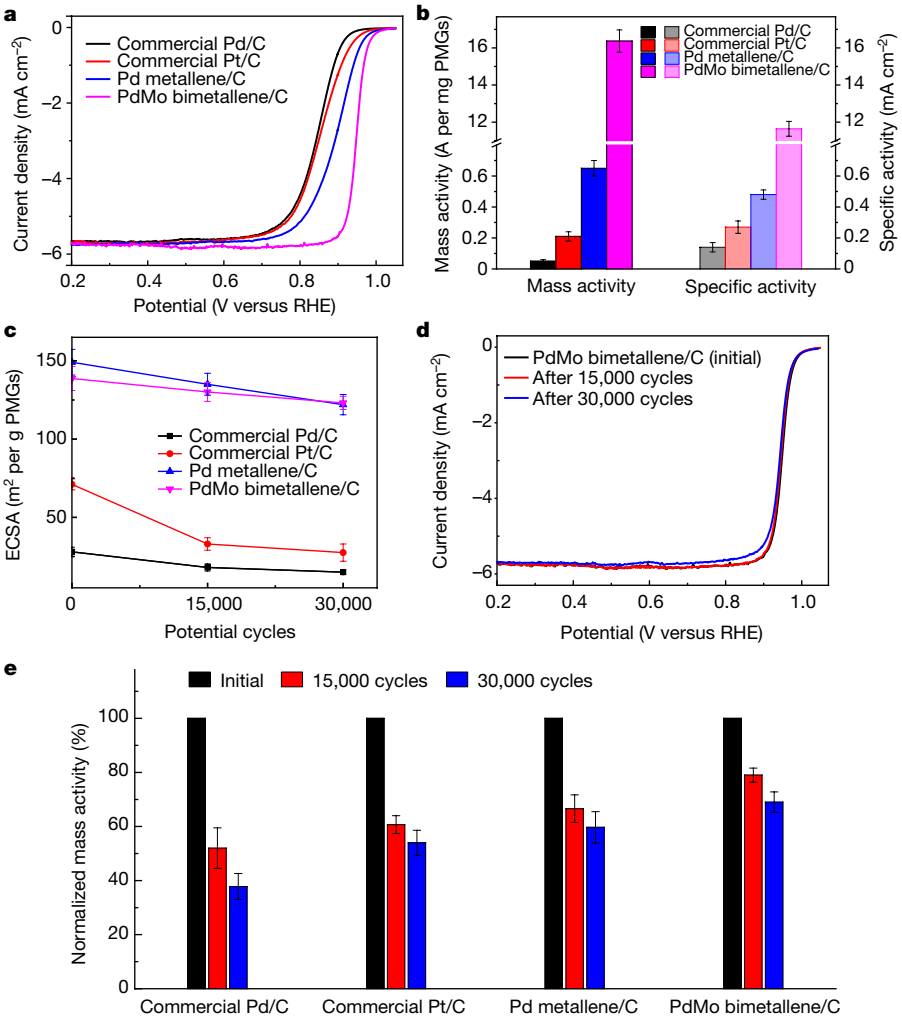

Fig. 2 | Electrocatalytic performance of PdMo bimetallene/C, Pd metallene/C, and the commercial catalysts Pt/C and Pd/C. a, **b**, ORR polarization curves (**a**) and a comparison of the mass and specific activities (**b**) of the stated catalysts in 0.1 M KOH at 0.9 V versus RHE. **c**–**e**, ECSAs (**c**), ORR polarization curves (**d**) and normalized mass activity changes (**e**) of the catalysts at their corresponding half-wave potentials $E_{1/2}$ (minimizing the influence from O_2-diffusion limitation) before and after 15,000 or 30,000 potential cycles. The error bars in **b**, **c** and **e** represent the standard deviations of at least three independent measurements of the same sample.

underpotentially depositing copper (Cu_{upd}) and Pd oxide reduction (Methods, Extended Data Fig. 4e–n). The ECSAs determined from the Cu_{upd} method were used for further analysis[25]. Notably, Pd metallene and PdMo bimetallene catalysts have an ECSA of 149.1 m^2 per gram of Pd and 138.7 m^2 per gram of Pd, respectively, owing to their suprathin character. The ORR polarization curves in Fig. 2a show that the PdMo bimetallene/C has a half-wave potential ($E_{1/2}$) of 0.95 V in 0.1 M KOH, which is higher than those of the commercial Pt/C (0.85 V) and Pd/C (0.84 V). To further quantify the intrinsic ORR activity, we obtained the kinetic current of each catalyst using the Koutecký–Levich equation (Methods). PdMo bimetallene/C delivers a mass activity of 16.37 A per milligram PGMs at the generally chosen value of 0.9 V versus the reversible hydrogen electrode (RHE). This activity is 77.9 and 327.4 times higher than that of commercial Pt/C and Pd/C catalysts, respectively (Fig. 2b). Owing to the fast kinetics of PdMo bimetallene/C, 0.9 V is too close to the diffusion-limiting region to provide a reliable kinetic current density, and we therefore assessed activities at 0.95 V to eliminate O_2-diffusion limitations[26]. As listed in Table 1, the mass activity of PdMo bimetallene/C is still 16.9 and 107.5 times greater than that of Pt/C and Pd/C, respectively. The number of electrons transferred for PdMo bimetallene/C was determined from the Levich plot to be 3.95 (Extended Data Fig. 4o, p), which suggests a four-electron pathway from O_2 to OH^-. To the best of our knowledge, the ORR activity that we report here for PdMo bimetallene/C in alkaline solution has not been achieved by any other nanomaterials under comparable conditions, including various platinum-based nanostructures and palladium nanosheets synthesized using other approaches (Extended Data Fig. 5). PdMo bimetallene/C also exhibits higher ORR activity

Table 1 | ORR performance of PdMo bimetallene/C, Pd metallene/C, commercial Pt/C and Pd/C catalysts

Catalyst	ECSA (m^2 per g PGM)	Half-wave potential (V)	Mass activity (A per mg PGM at 0.9 V)	Specific activity (mA cm^{-2} at 0.9 V)	Mass activity (A per mg PGM at 0.95 V)	Specific activity (mA cm^{-2} at 0.95 V)
PdMo bimetallene/C	138.7 ± 9.1	0.95	16.37 ± 0.60	11.64 ± 0.40	0.645 ± 0.02	0.458 ± 0.009
Pd metallene/C	149.1 ± 8.2	0.89	0.65 ± 0.05	0.48 ± 0.03	0.104 ± 0.010	0.076 ± 0.007
Pt/C	71.1 ± 3.5	0.85	0.21 ± 0.03	0.27 ± 0.04	0.038 ± 0.005	0.049 ± 0.004
Pd/C	28 ± 3.0	0.84	0.05 ± 0.01	0.14 ± 0.03	0.006 ± 0.001	0.016 ± 0.002

The errors represent the standard deviations of at least three independent measurements of the same sample.

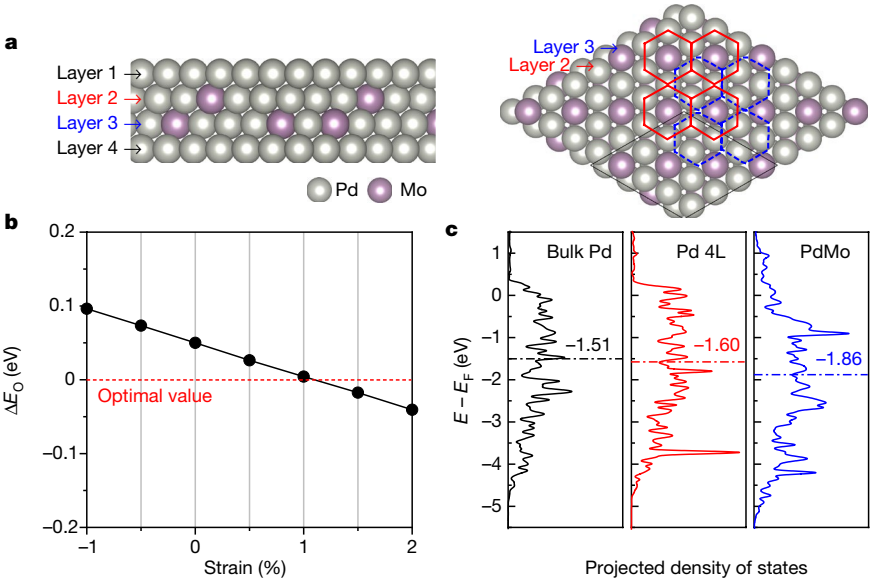

Fig. 3 | DFT calculations of oxygen adsorption energy and *d*-band centres. a, Left, side view of the atomic model of the four-layer PdMo bimetallene. Right, top view of the atomic model showing layers 2 and 3. In layers 2 and 3, each molybdenum atom is surrounded by six palladium atoms, indicated by the red (layer 2) and blue (layer 3) hexagons. **b**, ΔE_O of PdMo bimetallene as a function of compressive (negative) and tensile (positive) strains. The horizontal red line indicates the optimal ΔE_O value. **c**, The projected electronic density of states of the *d*-band for the surface palladium atoms in bulk Pd, a four-layer Pd sheet (Pd 4L) and PdMo. The horizontal dashed lines indicate the calculated *d*-band centre.

than the benchmark Pt/C in acid electrolytes, but its stability is not sufficient for practical applications (Extended Data Fig. 6).

Electrochemical durability in alkaline electrolytes was further assessed by conducting accelerated stability tests between 0.6 and 1.0 V versus RHE at 50 mV s^{-1} in O_2-saturated 0.1 M KOH. ECSAs measured before and after 15,000 and 30,000 potential cycles (Fig. 2c) remain high for both Pd metallene/C and PdMo bimetallene/C catalysts, and drop notably for the Pt/C and Pd/C controls. The loss of ECSA for the control catalysts can be ascribed to the increase in particle size (Extended Data Fig. 7a–h) as a result of nanoparticulate mobility, aggregation and Ostwald ripening[27]. PdMo bimetallene/C outperforms the other catalysts by retaining more of its initial mass activity after 30,000 cycles, and the ORR polarization curves obtained before and after the accelerated stability tests almost overlap (Fig. 2d, e). Furthermore, the initial morphology and structure of PdMo bimetallene was well maintained after accelerated stability tests (Extended Data Fig. 7i–l). We attribute the enhanced ORR durability of PdMo bimetallene to the large lateral size of its 2D nanostructure, the presence of multiple anchoring points between the bimetallene and the carbon support, a minimal proportion of under-coordinated surface atoms on the edges or vertices[28], and the electronic interaction with molybdenum rending surface palladium atoms less oxophilic (Fig. 1i, Extended Data Fig. 4a, b).

Density functional theory (DFT) calculations were performed to elucidate the origin of the enhancement in ORR activities induced by metallene catalysts. We constructed a four-atomic-layer model for PdMo bimetallene and calculated the oxygen adsorption energy (E_O), a widely used ORR activity descriptor that has an optimal value when the ORR activity reaches the maximum[29,30]. The atomic proportion of molybdenum in layers 2 and 3 and in layers 1 and 4 of the bimetallene model is 25% and 0%, respectively; this yields a total molybdenum content of 12.5% and is consistent with experimental results. Extensive DFT calculations were performed to determine the most stable atomic configurations in layers 2 and 3, and the results are shown in Fig. 3a. We calculated ΔE_O of PdMo bimetallene as a function of bi-axial strain, and the results are summarized in Fig. 3b. We find that ΔE_O reaches the optimal value at around 1% tensile strain; this suggests that the tensile strain is beneficial to ORR activity, which is consistent with the results of XRD and EXAFS experiments. In addition, there is substantial charge transfer from the molybdenum substrate to palladium on the top and the bottom surfaces (0.89*e* per molybdenum atom). As shown in Fig. 3c, the transferred electrons fill the *d*-band (the antibonding states) of the surface palladium atoms, shifting the centre of the band towards negative energy by 0.26 eV relative to the pure four-layer Pd sheet. The downshift of the *d*-band centre relieves the over-binding of oxygen on the surface, and moves ΔE_O towards the optimal value. There is also a downshift of the *d*-band centre (around 0.09 eV) of the four-layer Pd sheet relative to bulk Pd, which suggests that the quantum size effect—albeit smaller—is also beneficial to ORR activity. We conclude that alloying, strain and quantum size effects all contribute to the enhanced ORR activity of PdMo bimetallene, with the alloying effect having the most important role. This conclusion is further supported by the fact that, among various Pd-based alloys, the ΔE_O of PdMo bimetallene is closest to the optimum value (Extended Data Fig. 1k).

In addition to its promising ORR activity, PdMo bimetallene/C also shows good OER activity: compared to the benchmark IrO_2 catalyst, it exhibits a 30-mV smaller overpotential at 10 mA cm^{-2} as well as enhanced durability (Extended Data Fig. 8a, b). In a proof-of-principle demonstration of its practical use, we leveraged the bifunctional oxygen electrocatalytic activity of PdMo bimetallene/C and used it as the cathode in an aqueous Zn–air battery (Extended Data Fig. 8c–m). In addition to a high open-circuit voltage of 1.483 V and a maximum power density of 154.2 mW cm^{-2}, the PdMo bimetallene-based battery delivers a much higher specific capacity and gravimetric energy density than the battery that uses benchmark IrO_2 + Pt/C as a catalyst (798 mAh per gram Zn and 1,043 Wh per kilogram Zn versus 499 mAh per gram Zn and 543 Wh per kilogram Zn, respectively). We also examined the rate capability of our PdMo bimetallene/C Zn–air battery at different current densities (Extended Data Fig. 8h), as well as its durability at different discharge depths (Extended Data Fig. 8i, j) and high current densities (50 and 75 mA cm^{-2}; Extended Data Fig. 8l–n), further illustrating the potential of this material as an air cathode for practical applications (Extended Data Table 1). PdMo/C bimetallene also shows enhanced performance in non-aqueous Li–air batteries in comparison to commercial graphite, Pt/C and RuO_2/C (Extended Data Fig. 9). Our synthetic approach realizes highly curved and sub-nanometre-thick nanosheets of a palladium–molybdenum alloy, on which efficient and stable oxygen electrocatalysis is achieved in alkaline conditions owing to combined strain, quantum size and alloying effects. Our findings call for further study of metallene materials for renewable energy electrocatalysis.

Online content

Any methods, additional references, Nature Research reporting summaries, source data, extended data, supplementary information, acknowledgements, peer review information; details of author contributions and competing interests; and statements of data and code availability are available at https://doi.org/10.1038/s41586-019-1603-7.

Received: 25 August 2017; Accepted: 19 July 2019;
Published online 25 September 2019.

1. Seh, Z. W. et al. Combining theory and experiment in electrocatalysis: Insights into materials design. *Science* **355**, eaad4998 (2017).
2. Jiao, Y., Zheng, Y., Jaroniec, M. & Qiao, S. Z. Design of electrocatalysts for oxygen- and hydrogen-involving energy conversion reactions. *Chem. Soc. Rev.* **44**, 2060–2086 (2015).
3. Debe, M. K. Electrocatalyst approaches and challenges for automotive fuel cells. *Nature* **486**, 43–51 (2012
4. Suen, N. T. et al. Electrocatalysis for the oxygen evolution reaction: recent development and future perspectives. *Chem. Soc. Rev.* **46**, 337–365 (2017).
5. Shao, M., Chang, Q., Dodelet, J. P. & Chenitz, R. Recent advances in electrocatalysts for oxygen reduction reaction. *Chem. Rev.* **116**, 3594–3657 (2016).
6. Nørskov, J. K., Bligaard, T., Rossmeisl, J. & Christensen, C. H. Towards the computational design of solid catalysts. *Nat. Chem.* **1**, 37–46 (2009).
7. Stamenkovic, V. R., Strmcnik, D., Lopes, P. P. & Markovic, N. M. Energy and fuels from electrochemical interfaces. *Nat. Mater.* **16**, 57–69 (2017).
8. Stephens, I. E., Rossmeisl, J. & Chorkendorff, I. Toward sustainable fuel cells. *Science* **354**, 1378–1379 (2016).
9. Luo, M. & Guo, S. Strain-controlled electrocatalysis on multimetallic nanomaterials. *Nat. Rev. Mater.* **2**, 17059–17072 (2017).
10. Escudero-Escribano, M. et al. Tuning the activity of Pt alloy electrocatalysts by means of the lanthanide contraction. *Science* **352**, 73–76 (2016).
11. Bu, L. et al. Biaxially strained PtPb/Pt core/shell nanoplate boosts oxygen reduction catalysis. *Science* **354**, 1410–1414 (2016).
12. Li, M. et al. Ultrafine jagged platinum nanowires enable ultrahigh mass activity for the oxygen reduction reaction. *Science* **354**, 1414–1419 (2016).
13. Strasser, P. et al. Lattice-strain control of the activity in dealloyed core–shell fuel cell catalysts. *Nat. Chem.* **2**, 454–460 (2010).
14. Perez-Alonso, F. J. et al. The effect of size on the oxygen electroreduction activity of mass-selected platinum nanoparticles. *Angew. Chem. Int. Ed.* **51**, 4641–4643 (2012).
15. Wakisaka, M. et al. Electronic structures of Pt–Co and Pt–Ru alloys for CO-tolerant anode catalysts in polymer electrolyte fuel cells studied by EC-XPS. *J. Phys. Chem. B* **110**, 23489–23496 (2006).
16. Lee, J. et al. XPS studies of superconducting Mo–Ru–Rh–Pd alloy. *J. Alloys Compd.* **298**, 291–294 (2000).
17. Huang, X. Q. et al. High-performance transition metal-doped Pt_3Ni octahedra for oxygen reduction reaction. *Science* **348**, 1230–1234 (2015).
18. Gilroy, K. D., Ruditskiy, A., Peng, H. C., Qin, D. & Xia, Y. Bimetallic nanocrystals: syntheses, properties, and applications. *Chem. Rev.* **116**, 10414–10472 (2016).
19. Huang, X. et al. Freestanding palladium nanosheets with plasmonic and catalytic properties. *Nat. Nanotechnol.* **6**, 28–32 (2011).
20. Saleem, F. et al. Ultrathin Pt–Cu nanosheets and nanocones. *J. Am. Chem. Soc.* **135**, 18304–18307 (2013).
21. Duan, H. et al. Ultrathin rhodium nanosheets. *Nat. Commun.* **5**, 3093–3101 (2014).
22. Yang, N. et al. Synthesis of ultrathin PdCu alloy nanosheets used as a highly efficient electrocatalyst for formic acid oxidation. *Adv. Mater.* **29**, 1700769–1700774 (2017).
23. van der Vliet, D. F. et al. Unique electrochemical adsorption properties of Pt-skin surfaces. *Angew. Chem. Int. Ed.* **51**, 3139–3142 (2012).
24. Stamenkovic, V. R. et al. Improved oxygen reduction activity on $Pt_3Ni(111)$ via increased surface site availability. *Science* **315**, 493–497 (2007).
25. Shao, M., Odell, J. H., Choi, S.-I. & Xia, Y. Electrochemical surface area measurements of platinum- and palladium-based nanoparticles. *Electrochem. Commun.* **31**, 46–48 (2013).
26. Chen, C. et al. Highly crystalline multimetallic nanoframes with three-dimensional electrocatalytic surfaces. *Science* **343**, 1339–1343 (2014).
27. Darling, R. M. & Meyers, J. P. Kinetic model of platinum dissolution in PEMFCs. *J. Electrochem. Soc.* **150**, A1523–A1527 (2003).
28. Lopes, P. P. et al. Relationships between atomic level surface structure and stability/activity of platinum surface atoms in aqueous environments. *ACS Catal.* **6**, 2536–2544 (2016).
29. Nørskov, J. K. et al. Origin of the overpotential for oxygen reduction at a fuel-cell cathode. *J. Phys. Chem. B* **108**, 17886–17892 (2004).
30. Stamenkovic, V. R. et al. Changing the activity of electrocatalysts for oxygen reduction by tuning the surface electronic structure. *Angew. Chem. Int. Ed.* **45**, 2897–2901 (2006).

METHODS

Synthesis of PdMo bimetallene and Pd metallene. In a typical synthesis of PdMo bimetallene, 10 mg $Pd(acac)_2$, 30 mg ascorbic acid, 4 mg $Mo(CO)_6$ and 5 ml oleylamine were mixed in a 20-ml glass vial, and subsequently ultrasonicated for 1 h to yield a homogeneous solution. The vial was then sealed and transferred into an oil bath at 80 °C for 12 h. After cooling to room temperature, the colloidal product was collected by centrifugation, and washed several times with a mixture of ethanol and cyclohexane to remove the excess oleylamine. The final product was dispersed in cyclohexane for further use.

For the synthesis of Pd metallene, 10 mg $Pd(acac)_2$ and 30 mg ascorbic acid were first dissolved in 5 ml oleylamine under sonication. The resulting homogeneous solution was transferred into a Teflon high-pressure vessel and saturated with 2 atm CO gas. The vessel was heated from room temperature to 80 °C and maintained for 12 h. The product was collected by centrifugation and washed thoroughly with an ethanol/cyclohexane mixture before being stored in cyclohexane for further use.

Synthesis of nanomaterials. The PtPb nanoplates, hierarchical PtNi nanowires, ultrathin PtNi nanowires and PVP-capped Pd nanosheets were synthesized using previously reported methods[11,31–33].

Characterization. PXRD patterns were collected on a Shimadzu XRD-6000 X-ray diffractometer using Cu Kα radiation ($\lambda = 0.15406$ nm). The operation voltage and current were 40 kV and 30 mA, respectively. TEM was conducted on an FEI Tecnai T20 transmission electron microscope at an acceleration voltage of 120 kV. HRTEM and TEM–EDX were conducted on a FEI Tecnai F20 transmission electron microscope at an acceleration voltage of 200 kV. HAADF-STEM was conducted on a JEOL-2100F with a probe aberration corrector at an acceleration voltage of 200 kV. AFM was performed in tapping mode with a Multimode Nanoscope IIIa SPA (Veeco Instruments, Bruker) under ambient conditions. Ultrasharp cantilevers with a diamond-like carbon tip (NSG01, NT-MDT) were used. The image was flattened using the NanoScope Analysis software (v. 1.40). The composition of each catalyst was measured by ICP–AES (710-ES, Varian). XPS experiments were carried out using a Kratos AXIS Supra/Ultra spectrometer. The UV–Vis–near IR absorption spectra of PdMo bimetallene (dispersed in cyclohexane) were obtained on a UH4150 spectrophotometer (Hitachi).

EXAFS experiment and data processing. EXAFS measurements at the Pd K edge in both transmission (for Pd foil) and fluorescence (for samples) mode were performed at beamline BL14W1[34] at the Shanghai Synchrotron Radiation Facility. The electron beam energy was 3.5 GeV, and the stored current was 260 mA (top-up). A 38-pole wiggler with a maximum magnetic field of 1.2 T inserted in the straight section of the storage ring was used. EXAFS data were collected using a fixed-exit double-crystal Si(311) monochromator. A Lytle detector was used to collect the fluorescence signal, and the energy was calibrated using the Pd foil. The photon flux at the sample position was 1.8×10^{11} photons per second. The raw data analysis was performed using the IFEFFIT software package according to the standard data analysis procedures[35]. The spectra were calibrated, averaged, pre-edge background-subtracted, and post-edge normalized using the Athena program in the IFEFFIT software package. The Fourier transformation of the k^2-weighted EXAFS oscillations, $k^2\chi(k)$, from k space to R space was performed over a range of 2.7–11.4 $Å^{-1}$ to obtain a radial distribution function. Data fitting was performed using the Artemis program in IFEFFIT.

Galvanic substitution experiment. To verify the position of molybdenum atoms in PdMo bimetallene, a galvanic substitution experiment was performed by mixing 5 mg as-synthesized PdMo bimetallene ($Mo^{3+} + 3e^- \leftrightarrow Mo^0$, $E^0 = -0.2$ V; $Pd^{2+} + 2e^- \leftrightarrow Pd^0$, $E^0 = +0.95$ V) and 2 mg $CuCl_2$ ($Cu^{2+} + 2e^- \leftrightarrow Cu^0$, $E^0 = +0.34$ V) in 10 ml ethanol for 5 h. Both ICP–AES and XPS results (Extended Data Fig. 1j) of the final products (denoted as PdMo-Cu) suggest that no galvanic replacements of molybdenum by copper occurred, further confirming that molybdenum is located in the interior rather than at the surface of the bimetallene.

Estimation of strain from PXRD and EXAFS. According to a previous definition, the strain of Pd nanocrystals, s(Pd), can be obtained by the following equation:

$$s(\mathrm{Pd}) = \frac{a_n - a_b}{a_b} \times 100\%$$

Where a_b is the lattice parameter of bulk Pd (that is, 0.3890; JCPDS no. 46-1043), and a_n is the lattice parameter of the corresponding Pd nanocrystal. As determined from the PXRD data, the lattice parameters for Pd/C, Pd metallene and PdMo bimetallene are 0.3889, 0.3928 and 0.3941, respectively. Therefore, Pd/C has a negligibly compressive strain of 0.02%, whereas the Pd metallene and PdMo bimetallene have distinctively tensile strain of 0.97% and 1.31%, respectively. Furthermore, EXAFS analysis reveals that Pd metallene (0.277 nm) and PdMo bimetallene (0.278 nm) have tensile strains of 1.09% and 1.46%, respectively (the lattice parameter of Pd foil is 0.274 nm).

Electrochemical measurements. We prepared the catalyst sample by depositing as-synthesized nanocrystals onto commercial carbon black. Taking the preparation of the carbon-supported PdMo bimetallene catalyst as an example, 10 mg PdMo metallene dispersed in 10 ml cyclohexane, and 40 mg Ketjen carbon in 40 ml cyclohexane were mixed, and subsequently sonicated for 60 min. After stirring for another 12 h, the final product was collected by centrifugation, washed three times with ethanol and dried at 80 °C overnight under ambient conditions. The obtained catalyst powder was further treated in 0.5 M acetic acid solution at 60 °C under an N_2 atmosphere for 2 h to remove excess surfactant before use. To prepare the catalyst ink for electrochemical tests, 1 mg of the above-obtained catalyst powder was dispersed into 1 ml of a solution containing 750 μl water, 245 μl isopropanol and 5 μl 5 wt% Nafion solution, and sonicated for 30 min in an ice-water bath. The yielded homogeneous catalyst ink was used to prepare the working electrode. Commercial Johnson-Matthey Pt/C catalyst (20 wt%, 3-nm Pt nanoparticles supported on carbon black) and commercial Aldrich Pd/C catalyst (10 wt%, 8-nm Pd nanoparticles supported on activated charcoal) were used as benchmarks.

Electrochemical tests were performed using a three-electrode system on a CHI660E electrochemical analyser (CHI Instruments) with a catalyst-coated glassy carbon electrode (5 mm diameter) mounted on a rotator (Pine Instruments) as the working electrode and a Pt wire as the counter electrode. Before catalyst coating, the glassy carbon electrode was polished with alumina polishing slurries and cleaned with ultrapure water. A leak-free saturated calomel electrode was used as the reference electrode, and all potentials in this study were reported on a RHE scale. Before each electrochemical measurement, a hydrogen evolution reaction/hydrogen oxidation reaction polarization curve of a Pt electrode was recorded for calibration. The electrolytes were 0.1 M $HClO_4$ and 0.1 M KOH. As-prepared catalyst ink (7.5 μl) was deposited on the glassy carbon electrode, yielding a metal loading of around 7.5 μg of precious metals per cm^2 geometric area. To obtain a well defined diffusion-limited current plateau, the metal loading for commercial Pd/C was controlled to be 15 μg Pd per cm^2 geometric area. Cyclic voltammograms (CVs) were recorded at 50 mV s^{-1} after the electrolyte was purged with nitrogen for at least 30 min. Before recording, several fast CVs (500 mV s^{-1}) were recorded to clean and stabilize the catalyst surface until steady-state was obtained. ORR polarization curves were recorded in O_2-saturated electrolyte at 20 mV s^{-1} and a rotating rate of 1,600 rpm. The recorded ORR curves were iR-corrected before calculating the kinetic current (I_k) via the Koutecký–Levich equation: $I_k = (I_{lim} \times I)/(I_{lim} - I)$, where I_{lim} is the limiting current, and I is the measured current at a given potential. For each catalyst, the specific activity and the mass activity were obtained by normalizing the kinetic current to the corresponding ECSA (determined from Cu stripping) and the precious metal loading, respectively. Accelerated durability tests were conducted by cycling between 0.6 V and 1.0 V versus RHE at 50 mV s^{-1} for 15,000 and 30,000 cycles.

The ECSAs of palladium-based catalysts were determined from charges associated with underpotentially deposited H (H_{upd}) and Cu (Cu_{upd}), the stripping of CO, and the Pd oxide reduction. The desorption peaks of H_{upd} from recorded CVs were used to calculate the ECSAs[36], assuming a charge density of 210 μC cm^{-2} (a value for the polyhedron) for one monolayer of hydrogen coverage on commercial Pt/C and Pd/C, and a charge density of 240 μC cm^{-2} (a value for the (111) surface) for one monolayer of hydrogen coverage on PdMo bimetallene/C and Pd metallene/C. For the Cu stripping experiments, a N_2-saturated solution containing 2 mM $CuSO_4$ and 0.05 M H_2SO_4 was used as the electrolyte. The potential was first held at 0.3 V versus RHE for 100 s to form a Cu_{upd} monolayer[37], and then CVs were obtained from 0.3 V to 1.0 V at 20 mV s^{-1}. The ECSAs were calculated by subtracting the background CVs that were collected in N_2-saturated 0.05 M H_2SO_4 at 20 mV s^{-1}, assuming a charge density of 470 μC cm^{-2}. For the CO stripping experiments, CO gas (99.99%) was first bubbled into 0.1 M $HClO_4$ while holding the working electrode potential at 0.1 V versus RHE for 10 min. After purging the above electrolyte with N_2 for at least 30 min, two CVs were recorded at a scan rate of 20 mV s^{-1}. The ECSAs were calculated from the charge of CO stripping[25] (the first CV) by subtracting the background charge (the second CV), assuming a charge density of 420 μC cm^{-2}. For Pd oxide reduction, the CVs of various palladium-based catalysts were recorded from 0.1 V to 1.25 V versus RHE at 50 mV s^{-1}. The oxide reduction peak at around 0.8 V was used to calculate the ECSAs[38], assuming a charge density of 424 μC per cm^2 Pd.

Each electrochemical measurement was conducted at least three times, and the corresponding standard deviations were obtained.

DFT models and calculations. We constructed a four-atomic-layer model for PdMo bimetallene and calculated oxygen adsorption energy (E_O) on its surface. E_O is defined as $E_O = E_{surf+O} - E_{surf} - \frac{E_{O_2}}{2}$, where E_{surf+O} and E_{surf} are the total energies of the surface with and without the oxygen adsorbate, respectively, and E_{O_2} is the total energy of an oxygen molecule. There exists an optimal value of E_O, for which the ORR activity reaches the maximum. Here, for convenience, we shifted the optimal E_O value to 0 eV and used ΔE_O to represent the difference of a given E_O value relative to this optimal reference. All atoms were allowed to relax in the PdMo model. A six-layer slab model was used to simulate the surfaces of Pt(111) and Pd(111). The atoms in the top three layers were fully relaxed while those in the last three layers were fixed to simulate the bulk. To avoid interactions between periodic images, a vacuum layer of 15 Å is added to the adjacent slabs in both models. Our DFT calculations were carried out using the Vienna ab initio simulation package[39].

The Perdew–Burke–Ernzerhof functional within the generalized gradient approximation[40] and the projector augmented wave pseudopotential[41] were used in the calculations. An energy cutoff of 400 eV was used for the plane-wave basis set. The Brillouin zone was sampled on the basis of the Monkhorst–Pack scheme[42] _ ENREF_6_ENREF_6 with a $3 \times 3 \times 1$ k-point mesh. The force convergence criterion for atomic relaxation was 0.02 eV Å^{-1}. Extensive DFT calculations were performed to determine the most stable atomic configurations in layers 2 and 3 of the PdMo model. We found that in these layers, molybdenum atoms are uniformly distributed in the plane, but they tend to avoid each other across the planes, resulting in an average nearest-neighbour Mo–Mo distance of 4.58 Å. We also note that the ORR activity on other bimetallenes—such as PdW, PdCu and PdNi, which have the same structure—is lower than that of PdMo bimetallene, owing to either an overshift or an undershift of the d-band centre induced by either excessive or insufficient charge transfer from the substrate to the surface palladium atoms (Extended Data Fig. 1k).

The classical molecular dynamics calculations were performed at 300 K using the LAMMPS package[43] with the NVT (canonical) ensemble and embedded atom model interatomic potential[44]. The number of simulated steps was greater than 400,000 with a time-step of 1 fs. A 50 × 50 nm PdMo nanosheet (around 150,000 atoms) was included in the molecular dynamics simulations. All nearest-neighbour sites in the distance between 2.25 Å and 3.25 Å were included in the evaluation of the average strain. For the nearest-neighbour sites i and j, the strain was defined as $\varepsilon_{ij} = d_{ij}/d_0 - 1$, where d_{ij} is the interatomic distance between i and j and d_0 is the equilibrium nearest-neighbour distance in bulk palladium.

Zn–air battery test. The performance of the Zn–air battery was evaluated in a electrochemical cell prepared in house, on a battery test system (LANHE CT2001A). The Zn–air battery is composed of PdMo bimetallene/C coated carbon paper as the air cathode, Zn plate (1 mm in thickness) as the anode, and 6 M KOH + 0.2 M $Zn(Ac)_2$ aqueous solution as the electrolyte. For the comparison, the carbon paper coated by commercial catalysts (20 wt% Pt/C:IrO_2 = 1:1, mass ratio) was also used as the cathode. The air electrode was prepared by spreading the as-prepared catalysts ink onto carbon paper with a loading amount of 1 mg per cm^2 geometric area and dried at 110 °C in vacuum overnight. A commercial blue light-emitting diode (LED; 2.5–3 V) was used as an electronic load. The specific capacity was obtained by normalizing mAh to the mass of consumed zinc during the long-term discharge process, and the energy density is equal to the obtained specific capacity multiplied by the average discharge voltage. Notably, all the measurements of Zn−air batteries were conducted in air rather than in a pure oxygen stationary atmosphere. The depth of discharge (DOD) value can be calculated with the following equation: DOD value = (DOD discharge time)/(full discharge time) × 100%. For the DOD test, the effective geometric surface areas of the oxygen cathode and zinc anode are 1.4 cm^2 and 1 cm^2, respectively, which corresponds to a current density of 10 mA cm^{-2} at the cathode and 14 mA cm^{-2} at the anode. To better directly and unambiguously reflect the stability of the PdMo bimetallene cathode as the bifunctional oxygen electrocatalyst in rechargeable Zn–air batteries, during the cycling under the deep-DOD condition, we used a zinc wire as the reference electrode to minimize the influence from zinc-anode polarization. We also compared the performance of our Zn–air battery with other representative examples from the literature[45–52] (Extended Data Table 1).

Li–air battery test. The electrochemical tests on Li–air batteries were carried out using 2,032 coin-type cells with holes on the cathode side. The cells were composed of a lithium metal tablet anode, one slice of glass microfibre separator (Whatman), 0.2 ml electrolyte and a prepared cathode (11 mm diameter). The batteries were assembled in an argon-filled glove box, and then installed into a chamber prepared in house. Before the measurements, the chambers were flushed with pure oxygen. Each measurement was begun after a 12-h open-circuit potential step to ensure equilibrium in the cell. The electrochemical measurements were carried out using a LAND cycler (CT2001A). The preparation of the cathodes was carried out as follows: A mixture containing 80 wt% of active material and 20 wt% of polyvinylidene fluoride as binder was well mixed by grinding, and then pressed onto carbon paper, which served as a current collector. Owing to the highly hydrophobic nature of carbon paper, the suspension remained on the surface and thus would not block the oxygen channels in the paper. The cathodes were then dried at 100 °C under vacuum for 24 h before use. The loading density of the active material was controlled at approximately 0.5 mg cm^{-2}. Lithium bis(trifluoromethanesulfonyl)imide in tetraethylene glycol dimethyl ether (1 M) was used as the electrolyte, and prepared in an argon-filled glove box with water and oxygen content below 0.8 ppm.

Data availability

The data that support the findings of this study are available from the corresponding author on reasonable request.

Code availability

The Vienna ab initio simulation package (VASP) used for the DFT calculations is available at https://www.vasp.at. The LAMMPS package used for the classical molecular dynamics simulations is available under a GNU Public License at https://lammps.sandia.gov.

31. Bu, L. et al. A general method for multimetallic platinum alloy nanowires as highly active and stable oxygen reduction catalysts. *Adv. Mater.* **27**, 7204–7212 (2015).
32. Jiang, K. et al. Efficient oxygen reduction catalysis by subnanometer Pt alloy nanowires. *Sci. Adv.* **3**, e1601705 (2017).
33. Li, Y. et al. Size-controlled synthesis of Pd nanosheets for tunable plasmonic properties. *CrystEngComm* **17**, 1833–1838 (2015).
34. Y H-S. et al. The XAFS beamline of SSRF. *Nucl. Sci. Tech.* **26**, 050102–050108 (2015).
35. Newville, M. IFEFFIT: Interactive XAFS analysis and FEFF fitting. *J. Synchrotron Radiat.* **8**, 322–324 (2001).
36. Paulus, U. A. et al. Oxygen reduction on high surface area Pt-based alloy catalysts in comparison to well defined smooth bulk alloy electrodes. *Electrochim. Acta* **47**, 3787–3798 (2002).
37. Okada, J., Inukai, J. & Itaya, K. Underpotential and bulk deposition of copper on Pd(111) in sulfuric acid solution studied by in situ scanning tunneling microscopy. *Phys. Chem. Chem. Phys.* **3**, 3297–3302 (2001).
38. Sheng, W., Myint, M., Chen, J. G. & Yan, Y. Correlating the hydrogen evolution reaction activity in alkaline electrolytes with the hydrogen binding energy on monometallic surfaces. *Energy Environ. Sci.* **6**, 1509–1512 (2013).
39. Kresse, G. & Furthmüller, J. Efficient iterative schemes for ab initio total-energy calculations using a plane-wave basis set. *Phys. Rev. B* **54**, 11169–11186 (1996).
40. Perdew, J. P., Burke, K. & Ernzerhof, M. Generalized gradient approximation made simple. *Phys. Rev. Lett.* **77**, 3865–3868 (1996).
41. Blöchl, P. E. Projector augmented-wave method. *Phys. Rev. B* **50**, 17953–17979 (1994).
42. Monkhorst, H. J. & Pack, J. D. Special points for Brillouin-zone integrations. *Phys. Rev. B* **13**, 5188–5192 (1976).
43. Plimpton, S. Fast parallel algorithms for short-range molecular dynamics. *J. Comput. Phys.* **117**, 1–19 (1995).
44. Zhou, X. W., Johnson, R. A. & Wadley, H. N. G. Misfit-energy-increasing dislocations in vapor-deposited CoFe/NiFe multilayers. *Phys. Rev. B* **69**, 144113–144123 (2004).
45. Li, Y. G. et al. Advanced zinc–air batteries based on high-performance hybrid electrocatalysts. *Nat. Commun.* **4**, 1805–1812 (2013).
46. Nam, G. et al. Carbon-coated core–shell Fe–Cu nanoparticles as highly active and durable electrocatalysts for a Zn–air battery. *ACS Nano* **9**, 6493–6501 (2015).
47. Cui, Z., Li, Y., Fu, G., Li, X. & Goodenough, J. B. Robust Fe_3Mo_3C supported IrMn clusters as highly efficient bifunctional air electrode for metal–air battery. *Adv. Mater.* **29**, 1702385–1702392 (2017).
48. Cui, Z., Fu, G., Li, Y. & Goodenough, J. B. Ni_3FeN-supported Fe_3Pt intermetallic nanoalloy as a high-performance bifunctional catalyst for metal–air batteries. *Angew. Chem. Int. Ed.* **56**, 9901–9905 (2017).
49. Liu, X. et al. Integrating NiCo alloys with their oxides as efficient bifunctional cathode catalysts for rechargeable zinc–air batteries. *Angew. Chem. Int. Ed.* **54**, 9654–9658 (2015).
50. Winther-Jensen, B., Winter-Jensen, O., Forsyth, M. & Macfarlane, D. High rates of oxygen reduction over a vapor phase-polymerized PEDOT electrode. *Science* **321**, 671–674 (2008).
51. Lee, J. S., Lee, T., Song, H. K., Cho, J. & Kim, B. S. Ionic liquid modified graphene nanosheets anchoring manganese oxide. *Energy Environ. Sci.* **4**, 4148–4154 (2011).
52. Zhang, J., Zhao, Z., Xia, Z. & Dai, L. A metal-free bifunctional electrocatalyst for oxygen reduction and oxygen evolution reactions. *Nat. Nanotechnol.* **10**, 444–452 (2015).

Acknowledgements This work was financially supported by the National Key R&D Program of China (number 2016YFB0100200), the National Natural Science Foundation of China (number 51671003), the Beijing Natural Science Foundation (number JQ18005), the BIC-ESAT project, the China Postdoctoral Science Foundation (number 2017M610022) and the Young Thousand Talents Program. The work at California State University Northridge was supported by the National Science Foundation PREM programme (DMR-1828019). The electron microscopy work used resources of the Center for Functional Nanomaterials, which is a US Department of Energy Office of Science Facility, at Brookhaven National Laboratory under contract number DE-SC0012704.

Author contributions S.G. supervised the research. S.G. and M.L. designed and performed most of the experiments and data analysis. Z.Z., X.Z. and G.L. performed the DFT simulations. Y.Z. conducted the Zn–air battery tests. S.G., D.S., S.H. and M.L. performed electron microscopy analysis. Y.X. conducted the Li–air battery tests. S.G. and M.L. co-wrote the paper. All authors discussed the results and assisted during manuscript preparation.

Competing interests The authors declare no competing interests.

Additional information

Correspondence and requests for materials should be addressed to S.G.

Peer review information *Nature* thanks Gu-Gon Park and Yun Zong for their contribution to the peer review of this work.

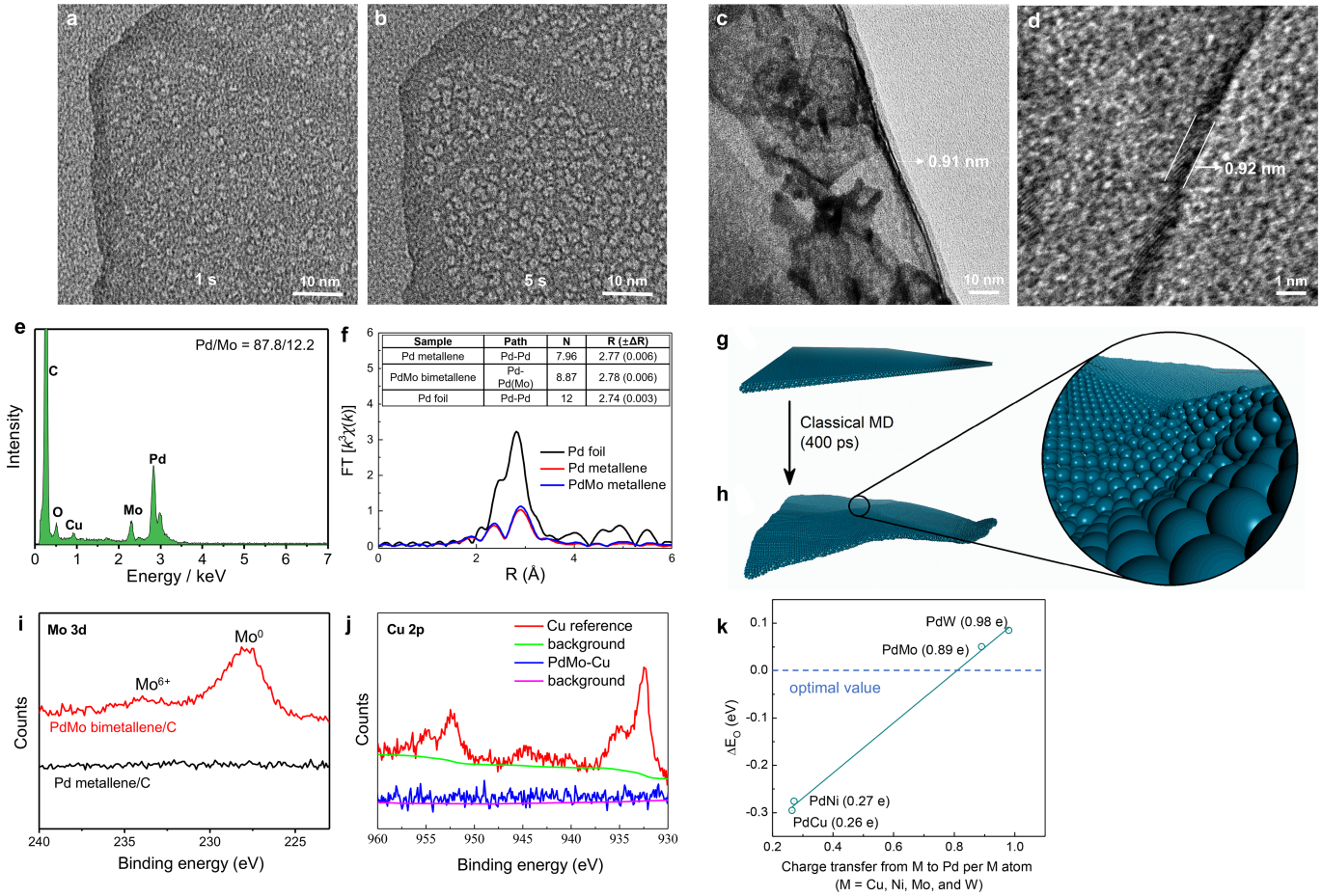

Extended Data Fig. 1 | Characterization of PdMo bimetallene. **a**, **b**, Representative HRTEM images of individual PdMo bimetallene nanosheets after exposure to the electron beam for 1 s (**a**) and 5 s (**b**). The observation of 'holes' after only a few seconds indicates the ultrathin nature of PdMo bimetallene. **c**, **d**, TEM (**c**) and HRTEM (**d**) images of the cross-section. **e**, TEM–EDX spectrum of PdMo bimetallene. **f**, The k^3-weighted $\chi(k)$-function of the EXAFS spectra for PdMo bimetallene (blue), Pd metallene (red) and Pd foil (black). The inset shows the results of EXAFS data fitting for different samples. The Pd–Pd(Mo) distance in the metallene samples is greater than that in the Pd foil, which suggests an expanded lattice for suprathin metallene materials; this is in good agreement with the results of XRD experiments and molecular dynamics simulations. **g**, **h**, The flat surface of PdMo bimetallene (**g**) is transformed to a wavy surface (**h**) after 400 ps in the molecular dynamics simulation. The inset shows an enlarged view of the centre of the nanosheet. **i**, Mo 3*d* core-level XPS spectra of the Pd metallene/C and PdMo bimetallene/C catalysts. **j**, Cu 2*p* core-level XPS spectra of PdMo-Cu and the Cu reference. The absence of Cu in the PdMo-Cu trace (blue) indicates there was no galvanic replacement of Mo with Cu^{2+}, confirming that Mo is located inside the metallene. **k**, The ΔE_O of PdMo, PdW, PdCu and PdNi as a function of charge transfer from other metals to Pd. PdMo bimetallene is the most active among all the PdM (M = Cu, Ni, Mo and W) materials tested, owing to the optimal charge transfer from Mo to the surface Pd atoms.

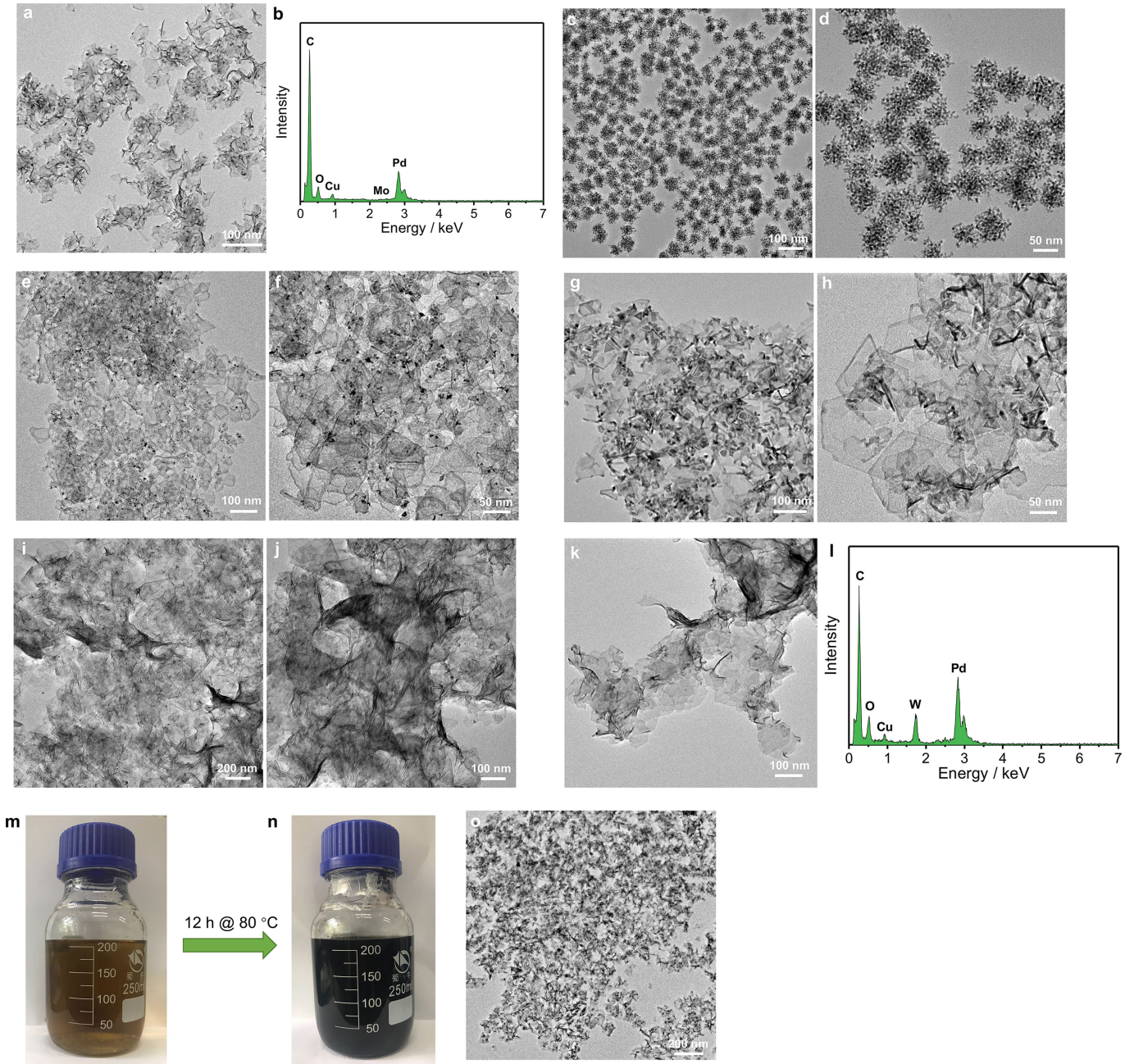

Extended Data Fig. 2 | Key characteristics of the synthesis. a, **b**, TEM image (**a**) and corresponding TEM-EDX spectrum (**b**) of the products obtained under the same reaction conditions as for PdMo bimetallene but in the absence of ascorbic acid. The absence of molybdenum in the as-obtained product suggests that ascorbic acid is crucial for the formation of the PdMo alloy. **c**, **d**, TEM images of the products obtained under the same reaction conditions as for PdMo bimetallene but in the absence of $Mo(CO)_6$. This observation confirms the essential role of CO molecules in the synthesis of ultrathin 2D nanostructures. **e**–**h**, TEM images of the products obtained under the same reaction conditions as for PdMo bimetallene except for the use of 8 mg $Mo(CO)_6$ (**e**, **f**) and 2 mg $Mo(CO)_6$ (**g**, **h**). **i**, **j**, TEM images of the products obtained under the same reaction conditions as for PdMo bimetallene, but with three times the concentration of metal precursors. The observations suggest that this approach can be used to tune the lateral size of the nanosheet. **k**, **l**, TEM image (**k**) and corresponding TEM–EDX spectrum (**l**) of the products obtained under the same reaction conditions as for PdMo bimetallene, except for the replacement of $Mo(CO)_6$ with $W(CO)_6$. **m**, **n**, Photographs of the colloids from a scale-up (40 times) synthesis of PdMo bimetallene before (**m**) and after (**n**) reaction. **o**, Typical TEM image of PdMo bimetallene from the scale-up synthesis.

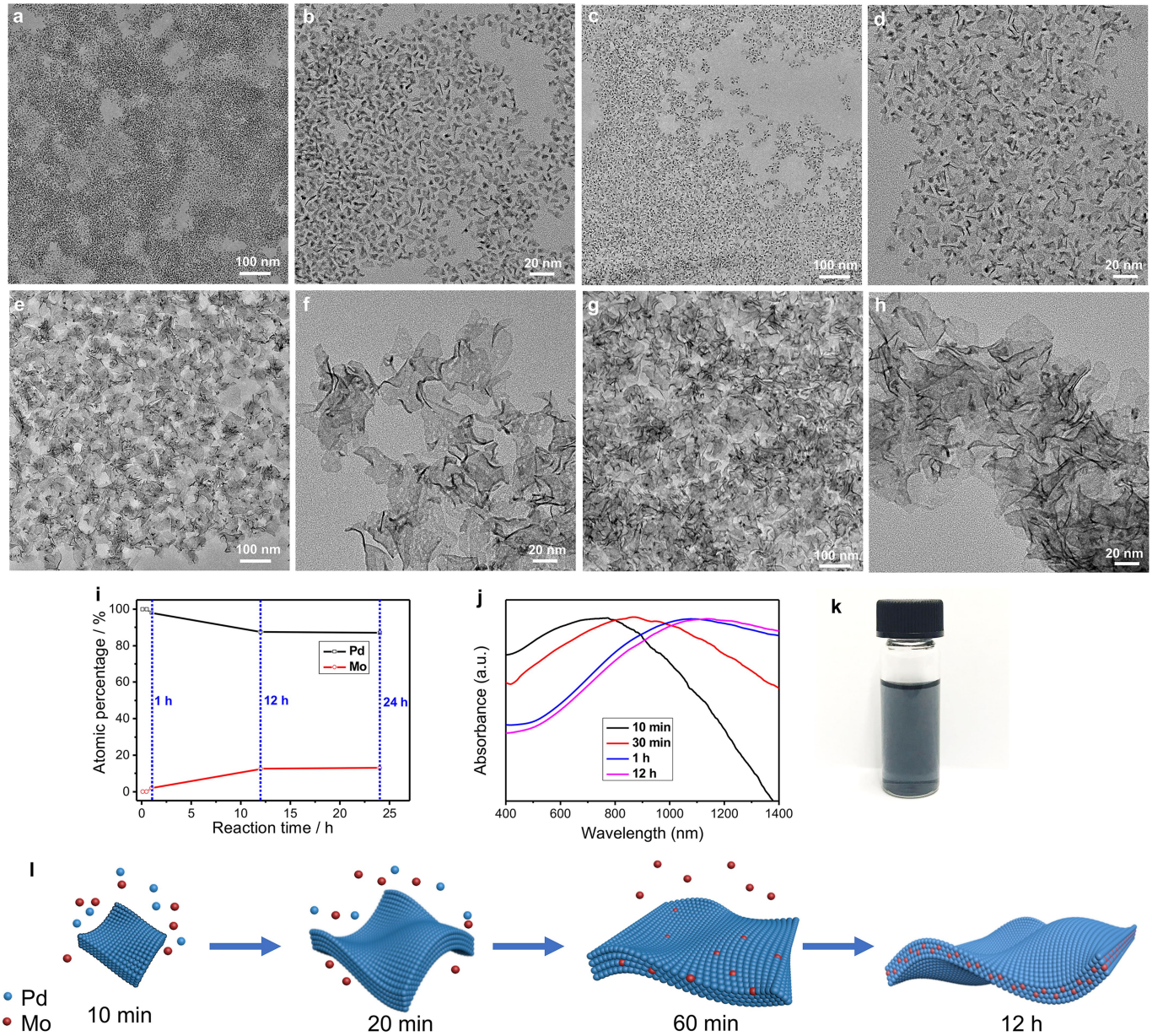

Extended Data Fig. 3 | Growth mechanism of PdMo bimetallene. **a**–**h**, Typical TEM images of PdMo bimetallene products collected after reaction times of 10 min (**a**, **b**), 20 min (**c**, **d**), 1 h (**e**, **f**) and 12 h (**g**, **h**). **i**, Changes in the atomic composition of PdMo bimetallene, determined by TEM–EDX and ICP–AES. **j**, UV–visible absorption spectra of PdMo bimetallene obtained at different reaction times. **k**, Photograph of a cyclohexane dispersion of the as-prepared PdMo bimetallene collected at 12 h. **l**, Synthetic scheme for the production of PdMo bimetallene. At the early stage of synthesis (10 min), the product contained nanocrystals with dimensions of only a few nanometres, with a definite 2D morphology. From 10 min to 20 min, the size of the nanocrystals gradually increased to tens of nanometres—the ICP–AES and TEM–EDX spectra revealed negligible amounts of molybdenum in these two intermediates, indicating these initial 2D nanocrystals were composed of pure palladium. As the reaction time increased to 60 min, curved nanosheets—with dimensions of hundreds of nanometres—were formed, accompanied by an obvious increase in molybdenum content. This suggests the rapid growth of palladium nanosheets and the slow incorporation of molybdenum during this period. When the reaction time was increased to 12 h, there was no substantial change in the dimensions of the nanosheets, suggesting that most of the palladium precursors were consumed in the first 60 min. The content of molybdenum, however, rapidly increased to around 12%, indicating the incorporation and interdiffusion of molybdenum atoms into the metallene.

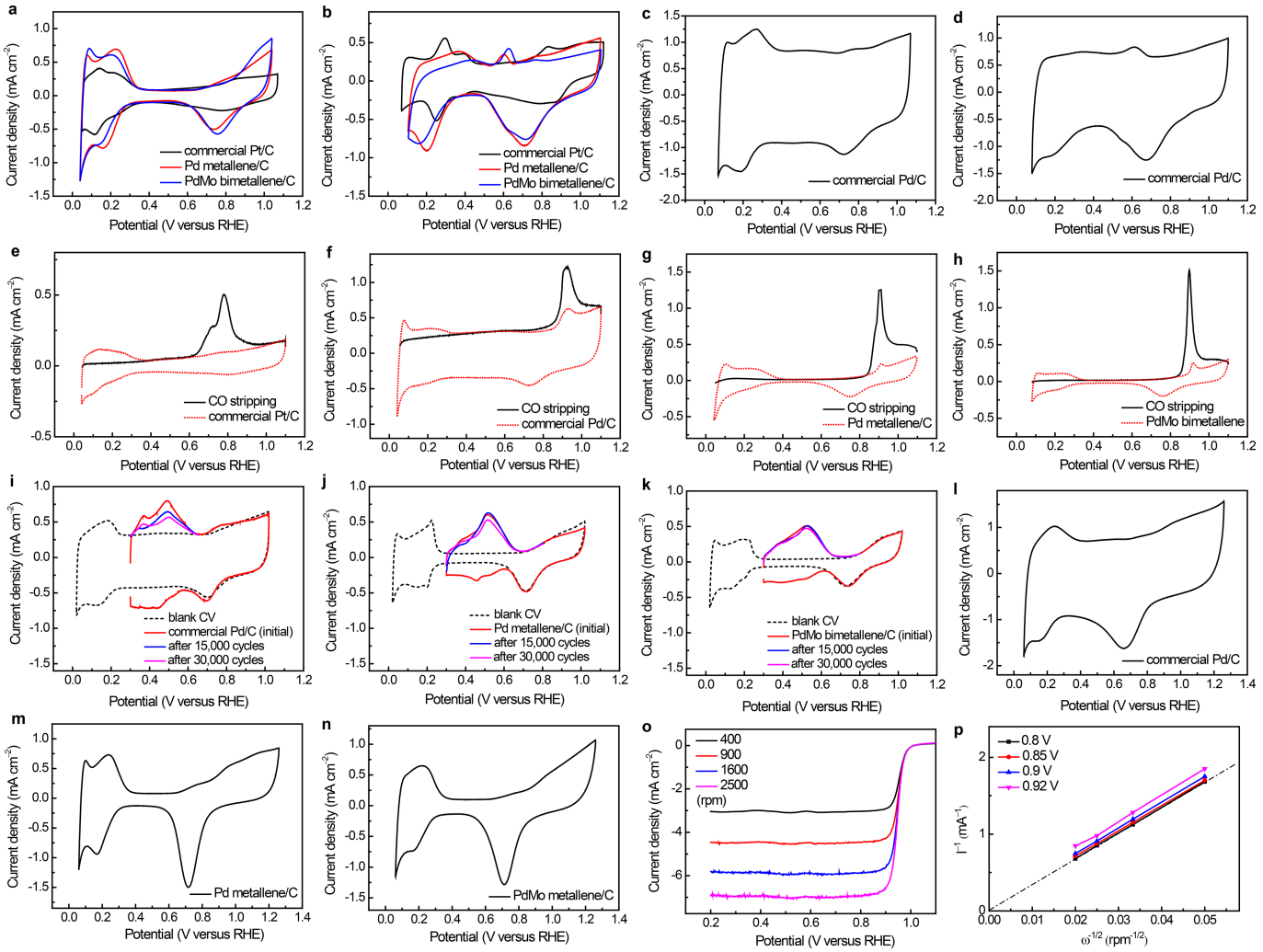

Extended Data Fig. 4 | Electrochemical properties of various catalysts. **a**, **b**, CVs of commercial Pt/C, Pd metallene/C and PdMo bimetallene/C catalysts in 0.1 M $HClO_4$ (**a**) and 0.1 M KOH (**b**). Scan rate, 50 mV s^{-1}; Pt (or Pd) loading, 7.5 mg per cm^2 geometric area. **c**, **d**, CVs of commercial Pd/C catalyst in **c**, 0.1 M $HClO_4$ and (**c**) 0.1 M KOH (**d**). Scan rate, 50 mV s^{-1}; Pt (or Pd) loading, 15 mg per cm^2 geometric area. **e**–**h**, CO stripping voltammograms of commercial Pt/C, commercial Pd/C, Pd metallene/C and PdMo bimetallene/C catalysts. The voltammograms were conducted in 0.1 M $HClO_4$. Scan rate, 20 mV s^{-1}. The integrated charge of CO stripping is used to calculate the ECSA of each catalyst. **i**–**k**, CVs and Cu stripping voltammograms of commercial Pd/C, Pd metallene/C and PdMo bimetallene/C catalysts before and after 15,000 and 30,000 potential cycles. The CVs were conducted in 0.05 M H_2SO_4, whereas the Cu stripping voltammograms were conducted in 0.05 M H_2SO_4 + 2 mM $CuSO_4$. Scan rate, 20 mV s^{-1}. The integrated charge of adsorbed Cu is used to calculate the ECSA of each catalyst before and after durability tests. **l**–**n**, CVs of commercial Pd/C, Pd metallene/C, and PdMo bimetallene/C catalysts in N_2-saturated 0.1 M $HClO_4$ solution. Scan rate, 50 mV s^{-1}. The integrated charge of oxide reduction is used to calculate the ECSA of each catalyst. **o**, ORR polarization curves of PdMo bimetallene/C in O_2-saturated 0.1 M KOH at different rotation rates. Scan rate, 20 mV s^{-1}. **p**, The corresponding Levich plots at different applied potentials.

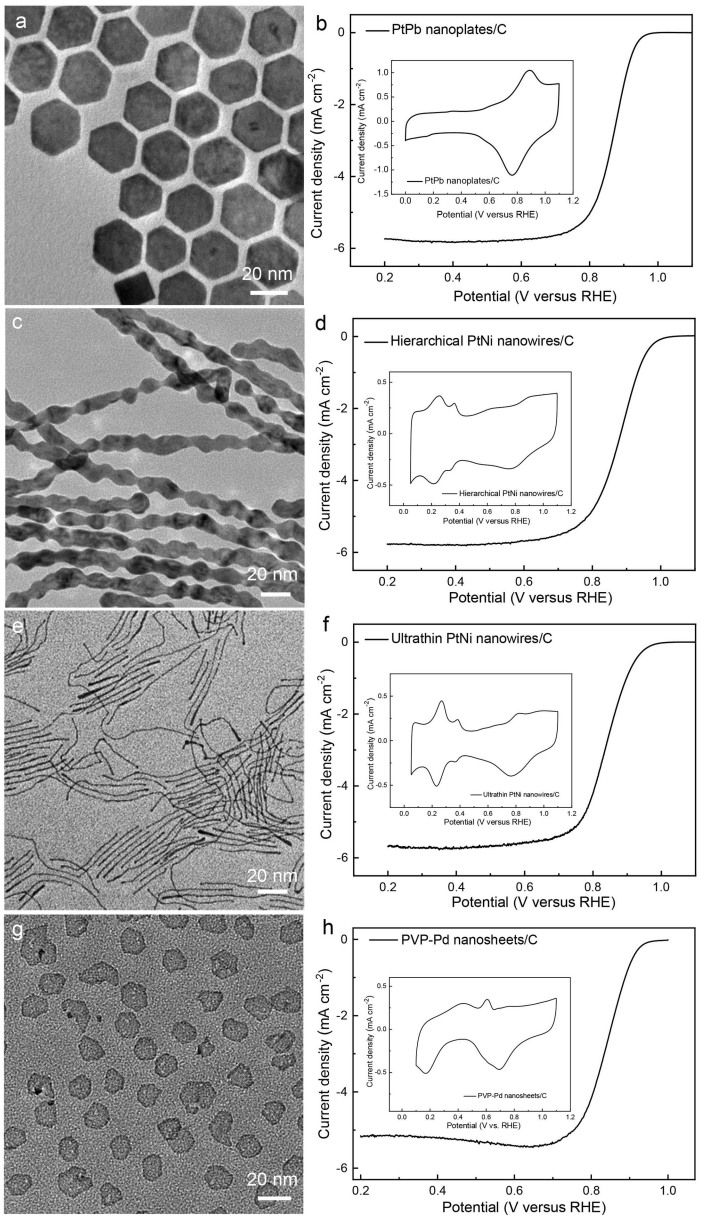

i

Catalyst	Mass activity @ 0.9 V (A mg^{-1}_{PMG})	Specific activity @ 0.9 V (mA cm^{-2})	$E_{1/2}$ (V)	References
PdMo bimetallene/C	16.37±0.6	11.64±0.4	0.95	This work
Pd metallene/C	0.65±0.05	0.48±0.03	0.89	This work
Commercial Pt/C	0.21±0.03	0.27±0.04	0.85	This work
Commercial Pd/C	0.05±0.01	0.14±0.03	0.84	This work
PtPb nanoplates/C	0.47	0.67	0.87	This work
PtNi h-NWs/C	0.32	1.05	0.88	This work
PtNi u-NWs/C	0.14	0.27	0.84	This work
CNT-Graphene	-	-	0.87	Nat. Nanotechnol. 2012, 7: 394.
Co_3O_4/N-rmGO hybrid	-	-	0.83	Nat. Mater. 2011, 10: 780.
N,P-mesoporous nanocarbon	-	-	0.85	Nat. Nanotechnol. 2015, 10: 444.
H-Pt/$CaMnO_3$	0.38 @ 0.85 V	1.05 @ 0.85 V	0.81	Adv. Mater. 2014, 26: 2047.
Pd_2NiAg	-	-	0.83	J. Am. Chem. Soc. 2015, 137: 2820.
Pd-P	1.34 @ 0.85 V	6.85 @ 0.85 V	0.88	J. Am. Chem. Soc. 2014, 136: 5217.
Au/$Cu_{40}Pd_{60}$ nanoparticles	0.43	-	~0.88	J. Am. Chem. Soc. 2014, 136: 15026.
Intermetallic AuCoPd	0.13	-	~0.85	Nat. Commun. 2014, 5: 5185.
Intermetallic CuCoPd/C	0.13	-	0.87	Angew. Chem. Int. Ed. 2016, 55: 9030.

Note: All potential values were given with respective to reversible hydrogen electrode (RHE) scale. The potentials were converted from Ag/AgCl (3 M KCl), $E_{RHE} = E_{Ag/AgCl} + 0.209\ V + 0.059 \times pH$; Ag/AgCl (saturated KCl), $E_{RHE} = E_{Ag/AgCl} + 0.197\ V + 0.059 \times pH$; saturated camel electrode, $E_{RHE} = E_{SCE} + 0.241\ V + 0.059 \times pH$; Hg/HgO electrode, $E_{RHE} = E_{MMO} + 0.098\ V + 0.059 \times pH$.

Extended Data Fig. 5 | Comparison of the performance of PdMo bimetallene/C with control samples and state-of-the-art catalysts from literature. a–h, TEM images (**a**, **c**, **e**, **g**) and ORR curves and CVs (inset) (**b**, **d**, **f**, **h**) of PtPb nanoplates (**a**, **b**), hierarchical PtNi nanowires (h-NWs; **c**, **d**), ultrathin PtNi nanowires (u-NWs; **e**, **f**), and PVP-capped Pd nanosheets (**g**, **h**). All CVs were recorded in N_2-saturated 0.1 M KOH at 50 mV s^{-1}, and the ORR polarization curves were recorded in O_2-saturated 0.1 M KOH at a scan rate of 20 mV s^{-1} and a rotation rate of 1,600 rpm. **i**, The table shows the ORR performance of PdMo bimetallene/C, in comparison with control catalysts in this study and other reported high-performance ORR catalysts in alkaline electrolytes.

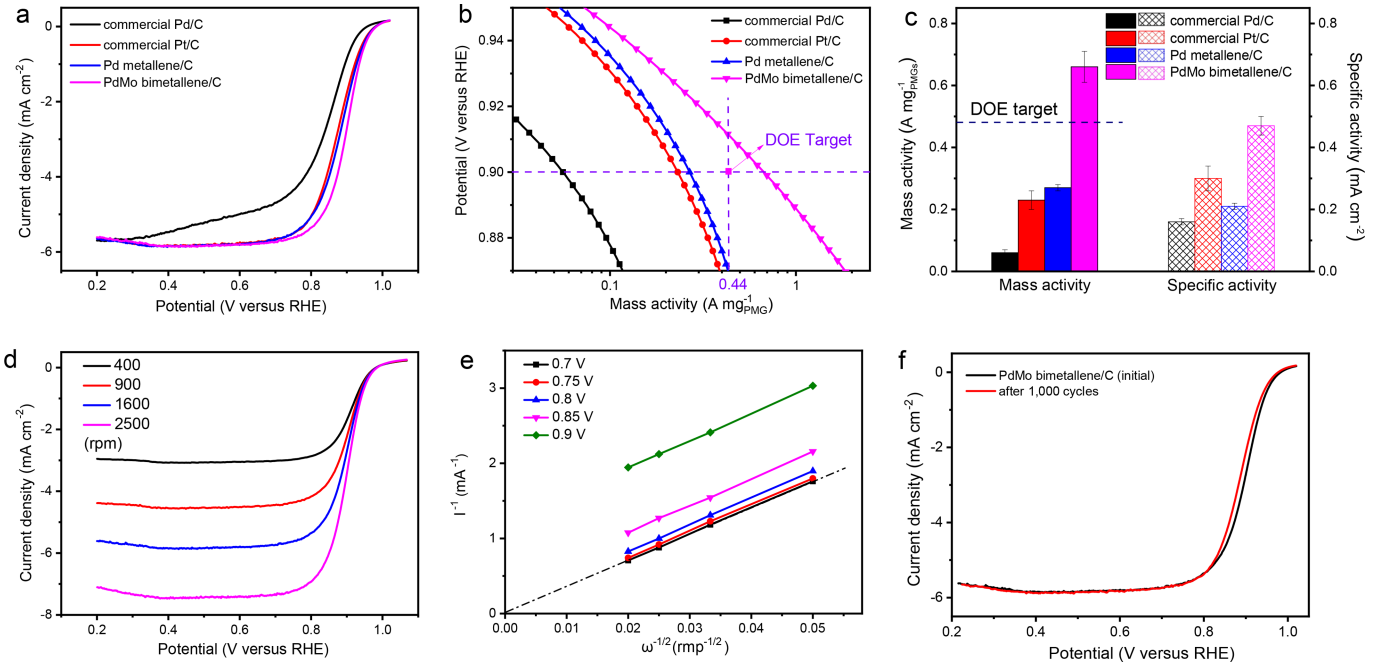

Extended Data Fig. 6 | ORR performance of various catalysts in acidic media. a–c, ORR polarization curves (**a**), corresponding Tafel plots (**b**) and mass- and specific activities (**c**) of commercial Pd/C, commercial Pt/C, Pd metallene/C and PdMo bimetallene/C catalysts. The dashed line in **c** and the purple square in **b** represent the 2020 technical target for mass activity set by the US Department of Energy. **d**, ORR polarization curves of PdMo bimetallene/C in O_2-saturated 0.1 M $HClO_4$ at different rotation rates. **e**, The corresponding Levich plots at different applied potentials. The ORR polarization curves were recorded in O_2-saturated 0.1 M $HClO_4$ at a scan rate of 20 mV s^{-1}. The error bars in **c** represent the standard deviations of at least three independent measurements of the same sample. The mass activity of PdMo bimetallene/C reaches 0.66 A per mg PGMs at 0.9 V versus RHE, around 3 and 10 times higher than those of commercial Pt/C and Pd/C, respectively, also exceeding the 2020 technical target set by the US Department of Energy (0.44 A per mg PGMs, indicated by the purple square in **b**. **f**, ORR polarization curves of PdMo bimetallene/C before and after AST for 1,000 cycles in O_2-saturated 0.1 M $HClO_4$.

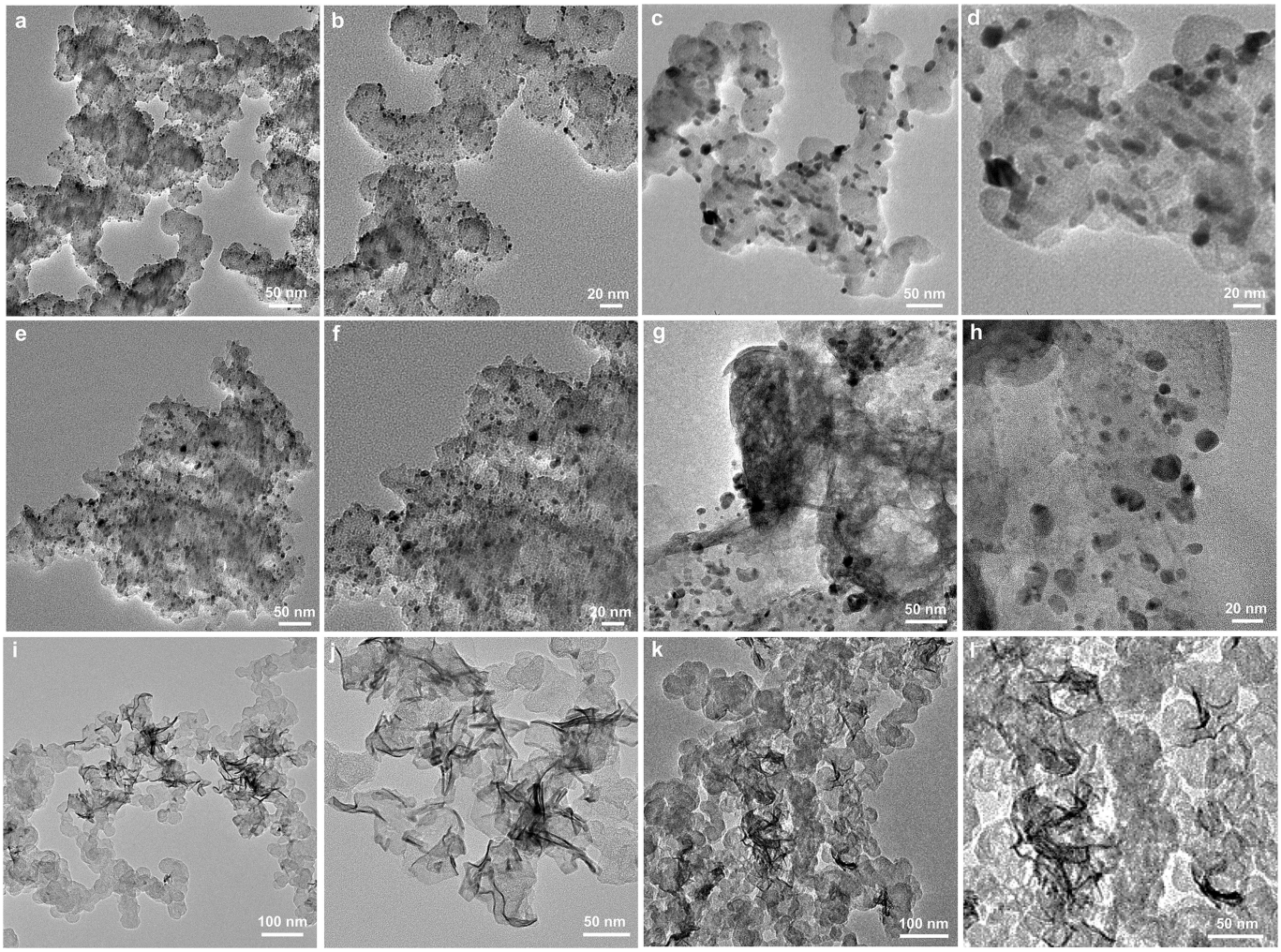

Extended Data Fig. 7 | Morphology changes of various catalysts after AST. a–l, Representative TEM images of commercial Pt/C catalyst (**a**–**d**), commercial Pd/C catalyst (**e**–**h**), and PdMo bimetallene/C catalyst (**i**–**l**) before (**a**, **c**, **e**, **g**, **i**, **k**) and after (**b**, **d**, **f**, **h**, **j**, **l**) 30,000 electrochemical cycles between 0.6 V and 1.0 V versus RHE, in O_2-saturated 0.1 M KOH at a scan rate of 50 mV s^{-1}.

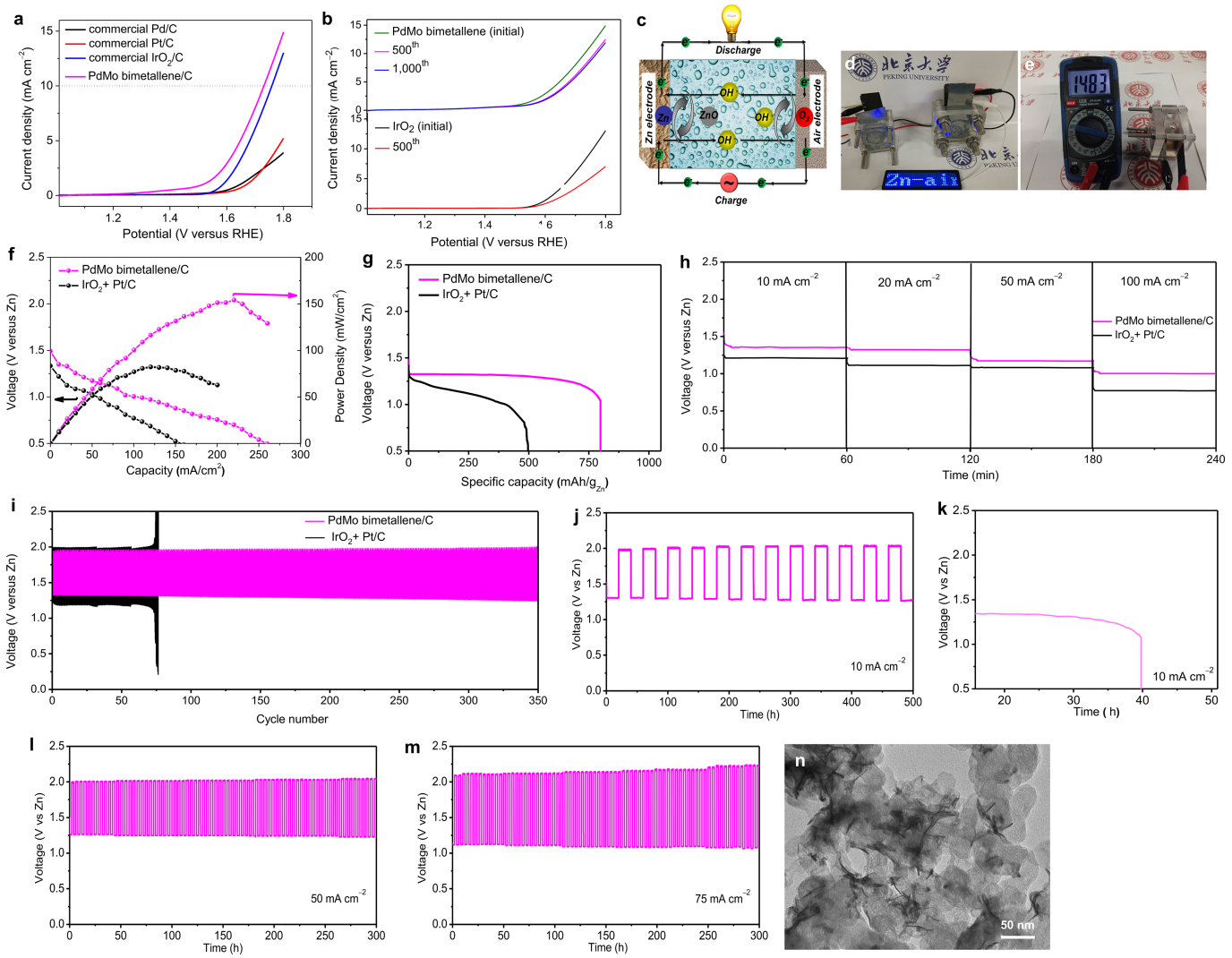

Extended Data Fig. 8 | OER electrocatalysis and performance of the Zn–air battery. a, OER polarization curves of various catalysts in O_2-saturated 0.1 M KOH at a scan rate of 5 mV s^{-1}. **b**, OER polarization curves of PdMo bimetallene and commercial IrO_2 before and after 500 or 1,000 cycles by cycling between 1.0 and 1.8 V versus RHE at a scan rate of 20 mV s^{-1}. **c**, Scheme of the aqueous Zn–air battery. **d**, LED panel (2.5–3 V) powered by two series-connected Zn–air batteries. **e**, An open-circuit voltage of 1.483 V was obtained for aqueous Zn–air batteries with PdMo bimetallene as air cathode. **f**, **g**, Polarization and corresponding power density curves (**f**) and consumed Zn mass-normalized specific capacities (**g**) of Zn–air batteries with PdMo bimetallene/C and IrO_2 + Pt/C as the cathodic catalysts at a current density of 20 mA cm^{-2}. **h**, Discharge curves of two Zn–air batteries at current densities of 10, 20, 50 and 100 mA cm^{-2}. **i**, Charge–discharge profiles of two Zn–air batteries at a current density of 10 mA cm^{-2} with each cycle being 20 min, corresponding to a shallow discharge depth. **j**, Galvanostatic charge–discharge cycling of a Zn–air battery using PdMo bimetallene/C as the air cathode at a charge density of 10 mA cm^{-2} with each cycle being 40 h, corresponding to a DOD of 51.0% (Methods; Zn wire as reference electrode). **k**, Full discharge profile (voltage versus hours of discharge) for a Zn–air battery using PdMo bimetallene/C as the air cathode at a current density of 10 mA cm^{-2}. **l**, **m**, Cycling stability of a Zn–air battery using PdMo bimetallene/C as the air cathode operating at current densities of 50 mA cm^{-2} (**l**) and 75 mA cm^{-2} (**m**) with each cycle being 4 h (Zn wire as reference electrode). **n**, TEM image of PdMo bimetallene/C after an operation period as the cathode of a Zn–air battery of 500 h.

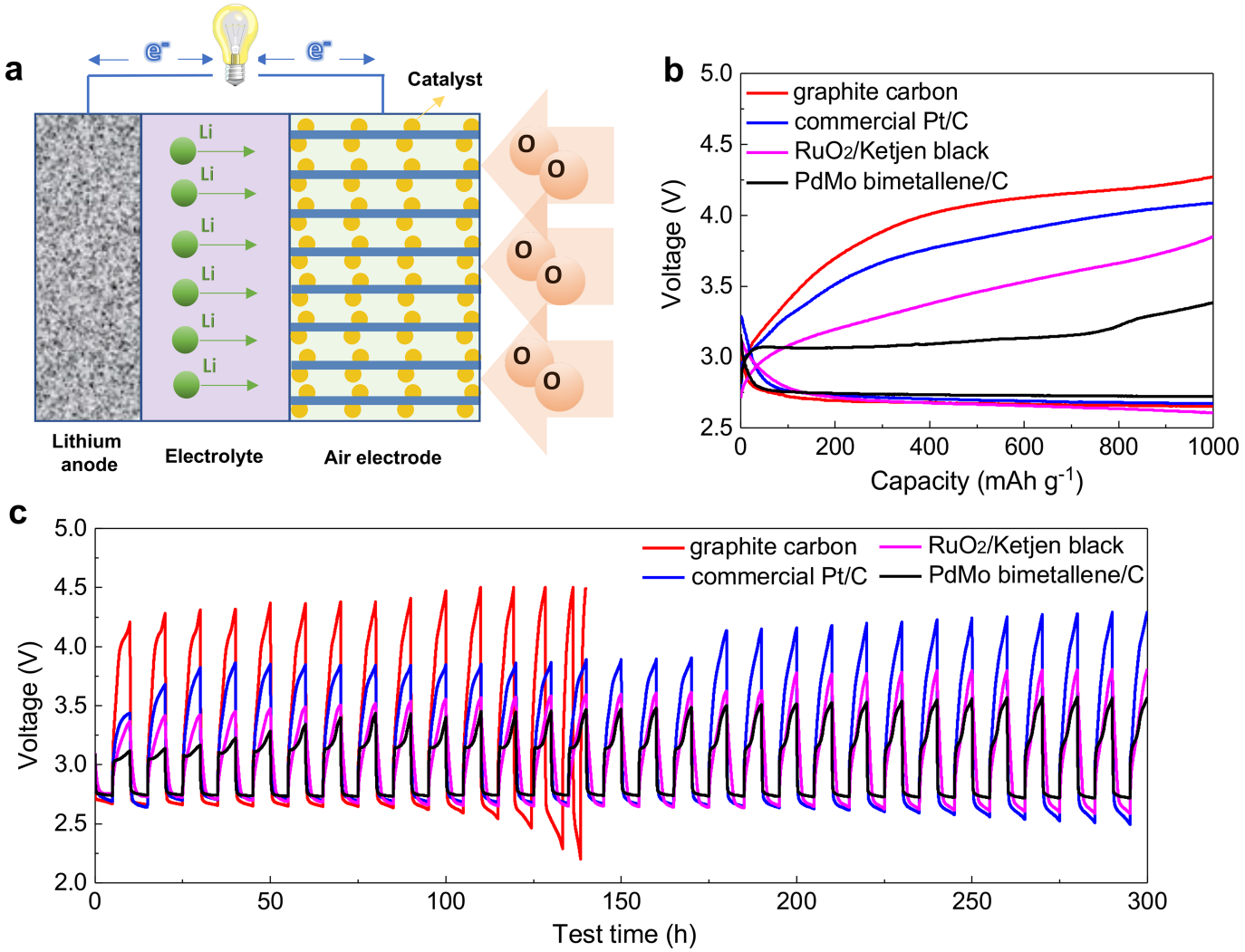

Extended Data Fig. 9 | Performance of the Li–air battery. a, Schematic of the configuration of the aprotic Li–air battery. A carbon paper coated with PdMo bimetallene/C, commercial Pt/C, RuO_2/Ketjen black or graphite carbon, a lithium plate, and 1 M LiTFSI in TEGDME were used as the cathodes, anode and electrolyte, respectively. **b**, The first discharge–charge profiles of Li–air batteries with various air electrodes recorded at a current density of 200 mA g^{-1} and a limited capacity of 1,000 mAh g^{-1}. **c**, The cycling performance of Li–air batteries with various air electrodes at a current density of 100 mA g^{-1} and a limited capacity of 500 mAh g^{-1}.

Extended Data Table 1 | Summary of the performance of the Zn–air battery prepared in this work and representative literature examples[45–52]

Air cathode	Catalysts loading (mg cm^{-2})	Open circuit voltage (V)	Specific capacity (mAh g^{-1}_{Zn})	Voltage @ 10 mA cm^{-2} (V)	Cycling condition and stability	References
PdMo bimetallene/C	1	1.483	798	1.35	20 min/cycle for 350 cycles, 0.13 V increase in overvoltage; 40 h/cycle for 12 cycles, 0.02 V increase in overpotential after 2 cycles, being stable for at least 500 h; 4 h/cycle for 300 h at 50 mA cm^{-2}, 1.21 V discharge voltage and 2.05 V charge voltage.	This work
Commercial Pt/C+IrO_2	1	1.361	499	1.21	20 min/cycle for 74 cycles; 0.26 V increase in overvoltage.	This work
CoO/N-CNT	1	~1.40	~570	-	20 h/cycle for 2 cycles; more than 0.2 V increase in overvoltage.	Reference (*45*)
CuFe@C	-	~1.35	-	~1.28	-	Reference (*46*)
IrMn@ Fe_3Mo_3C	10	-			120 min/cycle for 100 cycles; ~0.11 V increase in overvoltage.	Reference (*47*)
Fe_3Pt/Ni_3FeN	10		-	~1.2	120 min/cycle for 240 cycles; 0.25 V increase in overvoltage.	Reference (*48*)
NCNT/CoO-NiO-NiCo	0.53	~1.22	594	1.22		Reference (*49*)
PEDOT	-	1.44	-	-	-	Reference (*50*)
Mn_3O_4/ graphene	-	--	-	1.23	-	Reference (*51*)
N, P doped nanocarbon	0.5	1.48	735	-	-	Reference (*52*)